Journal of Atmospheric Chemistry **47:** 107–138, 2004.

Photochemistry in the Arctic Free Troposphere: Ozone Budget and Its Dependence on Nitrogen Oxides and the Production Rate of Free Radicals

CRAIG STROUD [1], SASHA MADRONICH [1], ELLIOT ATLAS [1], CHRISTOPHER CANTRELL [1], ALAN FRIED [1], BRIAN WERT [1], BRIAN RIDLEY [1], FRED EISELE [1, 2], LEE MAULDIN [1], RICHARD SHETTER [1], BARRY LEFER [1], FRANK FLOCKE [1], ANDY WEINHEIMER [1], MIKE COFFEY [1], BRIAN HEIKES [3], ROBERT TALBOT [4] and DONALD BLAKE [5]

[1] *Atmospheric Chemistry Division, National Center for Atmospheric Research, 1850 Table Mesa Drive, Boulder, CO 80303, U.S.A., e-mail: cstroud@acd.ucar.edu*
[2] *Earth and Atmospheric Science Department, Georgia Institute of Technology, Atlanta, GA, U.S.A.*
[3] *School of Oceanography, University of Rhode Island, Narragansett, RI, U.S.A.*
[4] *Institute for the Study of Earth, Oceans and Space, University of New Hampshire, Durham, NH, U.S.A.*
[5] *Department of Chemistry, University of California, Irvine, CA, U.S.A.*

(Received: 23 December 2002; accepted: 13 November 2003)

Abstract. Local ozone production and loss rates for the arctic free troposphere (58–85° N, 1–6 km, February–May) during the Tropospheric Ozone Production about the Spring Equinox (TOPSE) campaign were calculated using a constrained photochemical box model. Estimates were made to assess the importance of local photochemical ozone production relative to transport in accounting for the springtime maximum in arctic free tropospheric ozone. Ozone production and loss rates from our diel steady-state box model constrained by median observations were first compared to two point box models, one run to instantaneous steady-state and the other run to diel steady-state. A consistent picture of local ozone photochemistry was derived by all three box models suggesting that differences between the approaches were not critical. Our model-derived ozone production rates increased by a factor of 28 in the 1–3 km layer and a factor of 7 in the 3–6 km layer between February and May. The arctic ozone budget required net import of ozone into the arctic free troposphere throughout the campaign; however, the transport term exceeded the photochemical production only in the lower free troposphere (1–3 km) between February and March. Gross ozone production rates were calculated to increase linearly with NO_x mixing ratios up to ~300 pptv in February and for NO_x mixing ratios up to ~500 pptv in May. These NO_x limits are an order of magnitude higher than median NO_x levels observed, illustrating the strong dependence of gross ozone production rates on NO_x mixing ratios for the majority of the observations. The threshold NO_x mixing ratio needed for net positive ozone production was also calculated to increase from $NO_x \sim 10$ pptv in February to ~25 pptv in May, suggesting that the NO_x levels needed to sustain net ozone production are lower in winter than spring. This lower NO_x threshold explains how wintertime photochemical ozone production can impact the build-up of ozone over winter and early spring. There is also an altitude dependence as the threshold NO_x needed to produce net ozone shifts to higher values at lower altitudes. This partly

explains the calculation of net ozone destruction for the 1–3 km layer and net ozone production for the 3–6 km layer throughout the campaign.

Key words: global atmospheric chemistry, TOPSE, arctic photochemistry, ozone production, peroxide, radical chain length.

1. Introduction

The seasonal cycle of ozone (O_3) in the free troposphere has been an area of continued interest in atmospheric chemistry over the past several decades (Logan, 1985; Levy *et al.*, 1985; Muller and Brasseur, 1995; Yienger, 1999; Reeves *et al.*, 2002). Measurements from surface stations and ozonesondes in the remote northern hemisphere have shown a distinct springtime maximum in tropospheric O_3 (Otlmans *et al.*, 1996; Monks *et al.*, 2000). Junge (1962) suggested that the mixing ratio of tropospheric O_3 is determined by transport of O_3 from the stratosphere and destruction at the ground. This theory was questioned by Chameides and Walker (1973) and Crutzen (1974) and it is now generally believed that photochemical production in the troposphere and transport from the stratosphere both have important roles in shaping the tropospheric distribution of O_3 (Levy *et al.*, 1985; Follows and Austin, 1992; Jacob *et al.*, 1996; Roelofs and Lelieveld, 1995; Mauzerall *et al.*, 1996; Levy *et al.*, 1997; Tanimoto *et al.*, 2002). O_3 photochemistry in the troposphere is highly sensitive to the mixing ratios of O_3 precursor gases (such as nitrogen oxides $NO_x = NO + NO_2$, H_2O, CO and hydrocarbons) whose distributions are highly variable in space and time. The 2000 Tropospheric Ozone Production about the Spring Equinox (TOPSE) aircraft campaign took place over the North American continent at mid-to-high latitudes, characterizing the distribution of O_3 and O_3 precursor gases during the winter-to-spring transition (Atlas *et al.*, 2002). A major goal of TOPSE was to assess our understanding of the tropospheric O_3 budget, and in particular to quantify the *in situ* O_3 production rates.

Constrained photochemical box models have been used successfully to understand how local photochemistry responds to environmental conditions and the concentrations of longer-lived species. For example, Chameides *et al.* (1987) presented sensitivity studies to show how O_3 production would change if mixing ratios of H_2O, CO, NO and O_3 were doubled. Models can also give estimates of the mixing ratios of species that react quickly and thus should be in steady-state with their environment. If measurements of the precursor gases and the reactive species are made, then model-measurement comparisons of the reactive species provide a test of our understanding of fast photochemistry (Ridley *et al.*, 1992; Crawford *et al.*, 1999; Frost *et al.*, 1999; Zanis *et al.*, 1999; Jaegle *et al.*, 2000). Models can also give estimates of species that are difficult to measure. For example, Levy (1971) used a steady-state photochemical model to estimate the concentrations of intermediate radical species (OH, HO_2), which have only recently been measured

quantitatively in the atmosphere (Eisele *et al.*, 1997; Brune *et al.*, 1995; Cantrell *et al.*, 2000; Kanaya *et al.*, 2001).

Here, we first evaluate the detailed photochemistry in a box model by making model-measurement comparisons for radical and non-radical intermediates. We address the assumption of steady-state and the applicability of steady-state model-measurement comparisons for peroxide intermediates, H_2O_2 and CH_3OOH. We then calculate the seasonal dependence of *in situ* gross O_3 production and loss rates during TOPSE using our photochemical box model constrained by median observations and compare our model results with two other box modeling approaches (Cantrell *et al.*, 2003; Wang *et al.*, 2003). We focus our analysis on air masses sampled in the arctic free troposphere (58–85° N, 1–6 km) during the winter to spring transition (February–May). We also look at the dependence of the gross O_3 production (P_{O_x}) and the *in situ* chemical cycling (radical chain length) on total radical production rates (P_{RO_x}) and NO_x mixing ratios. We conclude by giving our assessment of the importance of the local tropospheric photochemical O_3 production to the seasonal trends in O_3 observed in the arctic free troposphere.

2. Methodology

2.1. DATA SORTING

The TOPSE campaign was composed of a series of seven round-trip deployments between 4 February 2002 and 23 May 2002 with missions generally sampling the mid-to-high latitude troposphere over North America in the corridor originating in Colorado, traversing over Manitoba and Hudson Bay before ending north of Greenland and returning back to Colorado. The National Center for Atmospheric Research C-130 aircraft was used to probe the chemical composition of the troposphere between 0–8 km. We based our analysis on a merged time series of the aircraft observations where the measurements were averaged over a common time interval of 1 minute. We sorted the observations based on latitude (40–50, 50–58, 58–85° N), altitude (0–1, 1–3, 3–6, 6–8 km) and month (February, March, April, May) and derived statistics (mean, 1σ standard deviation about the mean, median) for sorted cases. We assume that sampled air masses are representative of the region and month of the flights. Tables I and II list the mean $\pm 1\sigma$ standard deviation and the median for many of the critical chemical species over the springtime transition in the arctic (58–85° N), separated for the 1–3 km and 3–6 km altitude layers. Descriptions of the analytical measurement techniques and references can be found in a TOPSE overview paper (Atlas *et al.*, 2002).

2.2. MODEL APPROACH

Our major objective in this paper is to present the chemical budget for O_x ($[O_x] = [O] + [O_3] + [NO_2]$) during the springtime transition in the arctic free troposphere. Our general approach was to calculate 24-hr average O_x production and loss rates

Table I. Statistics generated from sorted aircraft data in the arctic mid-troposphere (58–85° N, 3–6 km)

Parameter	February Mean ± Std	Median	March Mean ± Std	Median	April Mean ± Std	Median	May Mean ± Std	Median
Latitude (°)	65 ± 5	64	71 ± 8	71	71 ± 8	72	71 ± 7	73
Altitude (km)	5.1 ± 0.8	5.5	5.0 ± 0.9	5.4	5.0 ± 0.8	5.1	4.8 ± 0.9	5.2
Temperature (K)	237 ± 8	236	239 ± 8	238	238 ± 7	237	246 ± 8	243
Water vapor (g/kg)	0.23 ± 0.33	0.08	0.29 ± 0.37	0.15	0.22 ± 0.24	0.14	0.32 ± 0.47	0.19
J_{O1D} (sec^{-1})	$9 \pm 7 \times 10^{-7}$	7×10^{-7}	$3 \pm 3 \times 10^{-6}$	3×10^{-6}	$6 \pm 5 \times 10^{-6}$	6×10^{-6}	$1.3 \pm 0.7 \times 10^{-5}$	1.2×10^{-5}
Surface albedo	0.82 ± 0.08	0.84	0.87 ± 0.03	0.87	0.84 ± 0.06	0.85	0.77 ± 0.09	0.78
Cloud factor	0.93 ± 0.19	0.98	0.97 ± 0.16	1.01	0.96 ± 0.07	0.97	0.95 ± 0.07	0.95
O_3 (ppbv)	55 ± 7	54	63 ± 13	60	67 ± 10	65	75 ± 11	78
NO_x (pptv)	20 ± 16	18	25 ± 22	21	17 ± 13	15	30 ± 13	30
PAN (pptv)	117 ± 37	111	199 ± 96	177	263 ± 195	222	319 ± 86	323
HNO_3 (pptv)	39 ± 24	34	58 ± 70	32	51 ± 57	37	76 ± 42	68
NO_y (pptv)	283 ± 89	279	352 ± 150	326	385 ± 234	332	436 ± 112	446
CH_4 (ppmv)	1.81 ± 0.01	1.81	1.83 ± 0.02	1.83	1.83 ± 0.01	1.86	1.83 ± 0.01	1.82
CH_2O (pptv)	100 ± 88	90	91 ± 92	73	47 ± 82	41	64 ± 68	55
H_2O_2 (pptv)	82 ± 81	58	115 ± 77	105	165 ± 67	168	180 ± 74	174
CH_3OOH (pptv)	113 ± 113	72	184 ± 121	157	126 ± 66	120	130 ± 64	125
CO (ppbv)	145 ± 11	146	154 ± 12	151	154 ± 9	154	145 ± 10	147
C_3H_6 (pptv)	589 ± 156	543	626 ± 255	607	398 ± 121	397	186 ± 43	179
CH_3CHO (pptv)	112 ± 42	104		140[a]	165 ± 101	141	183 ± 97	160
$CH_3C(O)CH_3$ (pptv)	381 ± 98	382		550[a]	692 ± 218	674	860 ± 214	839

[a] Estimate due to lack of data.

Table II. Statistics generated from sorted aircraft data in the arctic lower free troposphere (58–85° N, 1–3 km)

Parameter	February Mean ± Std	Median	March Mean ± Std	Median	April Mean ± Std	Median	May Mean ± Std	Median
Latitude (°)	67 ± 7	65	70 ± 9	74	68 ± 8	68	69 ± 9	72
Altitude (km)	2.0 ± 0.6	2.1	2.1 ± 0.6	2.2	2.1 ± 0.6	2.1	1.9 ± 0.5	1.8
Temperature (K)	252 ± 7	249	255 ± 8	253	258 ± 7	256	264 ± 5	266
Water vapor (g/kg)	0.68 ± 0.81	0.43	1.0 ± 1.1	0.57	0.89 ± 0.79	0.70	1.0 ± 0.6	0.93
J_{O1D} (sec^{-1})	$4 \pm 4 \times 10^{-7}$	3×10^{-7}	$3 \pm 3 \times 10^{-6}$	2×10^{-6}	$6 \pm 5 \times 10^{-6}$	6×10^{-6}	$1 \pm 1 \times 10^{-5}$	1×10^{-5}
Surface albedo	0.82 ± 0.08	0.84	0.87 ± 0.03	0.87	0.86 ± 0.06	0.86	0.78 ± 0.10	0.79
Cloud factor	0.94 ± 0.16	0.98	0.96 ± 0.15	1.01	0.97 ± 0.14	1.00	0.96 ± 0.16	1.01
O_3 (ppbv)	46 ± 4	45	53 ± 5	53	55 ± 6	54	56 ± 12	57
NO_x (pptv)	11 ± 15	7	25 ± 30	15	18 ± 17	13	28 ± 17	27
PAN (pptv)	158 ± 135	117	210 ± 106	197	199 ± 83	170	195 ± 98	172
HNO_3 (pptv)	69 ± 230	34	65 ± 61	39	81 ± 80	52	103 ± 52	96
NO_y (pptv)	301 ± 168	255	342 ± 161	310	309 ± 137	272	294 ± 142	265
CH_4 (ppmv)	1.84 ± 0.02	1.84	1.84 ± 0.01	1.84	1.84 ± 0.01	1.84	1.83 ± 0.01	1.83
CH_2O (pptv)	143 ± 160	106	166 ± 193	91	121 ± 150	48	93 ± 71	84
H_2O_2 (pptv)	45 ± 58	12[a]	152 ± 118	124	261 ± 151	235	340 ± 209	314
CH_3OOH (pptv)	94 ± 108	70	145 ± 78	140	187 ± 103	168	253 ± 115	251
CO (ppbv)	164 ± 19	161	156 ± 11	153	156 ± 5	156	144 ± 8	144
C_3H_6 (pptv)	920 ± 248	909	806 ± 176	780	448 ± 162	464	175 ± 43	166
CH_3CHO (pptv)	122 ± 43	107	153 ± 69	138	155 ± 61	140	218 ± 140	205
$CH_3C(O)CH_3$ (pptv)	426 ± 164	385	543 ± 203	502	621 ± 170	582	772 ± 140	732

[a] Half the estimated detection limit.

for different months and altitudes by using the photochemical box model constrained by the measured medians listed in Tables I and II. A median value could not be calculated for several reactive hydrocarbons due to instrument detection limits and a value of half the detection limit was used as a model constraint (e.g., n-octane had a detection limit of 3 pptv and was above detection limit for 5% of the samples). The photochemical box model was run over repetitive diurnal solar cycles to diel steady-state with photolysis frequencies (j values) calculated using the Tropospheric Ultraviolet Visible (TUV) radiative transfer code (Version 4; Madronich and Flocke, 1998). The TUV module was initialized with measured median values for latitude, Julian day, altitude, O_3 column and albedo. A standard aerosol vertical distribution was assumed to prescribe aerosol optical depths (Elterman, 1968). Cloud correction factors were calculated by comparing the TUV clear-sky modeled results run on individual aircraft points and individual j value measurements. Median values of the sorted cloud correction factors were then applied to all the j values calculated by TUV within the photochemical box model. The median $j(NO_2)$ and $j(O^1D)$ cloud correction factor ranged between 0.82–1.06 and 0.92–1.00, respectively, for the arctic free troposphere sampled during TOPSE. The TUV module was updated with cross section and quantum yields from recent evaluations for inorganic species (Demore *et al.*, 1997; Sander *et al.*, 2000) and organic species (Atkinson, 1997b; Atkinson *et al.*, 2000).

NCAR's master mechanism was used as the chemical scheme within the model (Madronich and Calvert, 1990). The inorganic chemistry has undergone updates since the original publication with the most recent recommendations taken from Demore *et al.* (1997); Sander *et al.* (2000). Hydrocarbon chemistry in the master mechanism is treated explicitly and includes the photo-oxidation of partly oxygenated organic species. Alkanes up to C_8, alkenes up to C_3 and aromatics up to C_8 were observed in the arctic free troposphere and were considered as initial hydrocarbon reagents in the gas-phase mechanism. The chemistry of the methyl peroxy radical is treated explicitly; a counter scheme is used for the other organic peroxy radicals (Madronich and Calvert, 1990). The rate coefficients for organic peroxy radical reactions were updated based on the recommendations in Tyndall *et al.* (2001) and Mereau *et al.* (2000). Alkoxy radical reactions were also updated based on the latest Demore *et al.* recommendation (for CH_3O) and the specific studies in Atkinson (1997) and Mereau *et al.* (2000) for the larger alkoxy radicals. OH initiation rate coefficients for hydrocarbons were updated based on the latest JPL compilations (Demore *et al.* 1997; Sander *et al.* 2000) and the Atkinson (1994) review. The OH-initiated ethene oxidation mechanism was modified to include multiple branching for the β-hydroxy ethoxy radical reaction with NO (Orlando *et al.*, 1998). OH-initiated rate coefficients for oxygenated hydrocarbons were updated from the Atkinson (1994) compilation.

The kinetics of the HO_2 self-reaction were recently measured by Christensen *et al.* (2002). The self-reaction proceeds via a complex potential energy surface and

displays pressure-dependent behavior. Demore *et al.* (1997) recommend separating the overall rate coefficient into two terms:

$$k_1 = k_0 + k'[\mathrm{M}], \tag{1}$$

where k_0 and k' are the bimolecular and termolecular components. Christensen *et al.* (2002) recommend, $k_0 = 1.5 \times 10^{-12}$ exp(19/T), compared to the Demore *et al.* recommendation, $k_0 = 2.3 \times 10^{-13}$ exp(600/T). As a result, the HO_2 self-reaction is considerably slower at the extreme cold temperatures found in the upper troposphere and stratosphere. Our photochemical box model results for arctic mid-troposphere (3–6 km) median conditions between February and May were compared. We found the impact of the new kinetic recommendation on HO_2, H_2O_2 and CH_3OOH mixing ratios was not significant for TOPSE conditions. At most, steady-state HO_2 was higher by 7%, H_2O_2 lower by 18% and CH_3OOH higher by 4% with the new recommendations.

Simulations were run for a time of 5 days, chosen in this study to allow sufficient initiation time for radical species to approach steady-state, but not so long as to allow several non-radical species in the model to reach unrealistic mixing ratios (e.g. H_2O_2, HNO_3). 5 days also represents a reasonable estimate for the amount of time an air mass sampled in the arctic free troposphere would experience uniform conditions. For model-measurement comparisons of intermediate species (H_2O_2, CH_3OOH and CH_2O), the species of interest was calculated while the other measured intermediates were constrained at their median values. For example O_3, H_2O, CO, NO_x, PANs, HNO_3, VOCs, CH_3OOH, CH_2O and CH_3CHO were held fixed at their median measured values during H_2O_2 time-varying simulations. Intermediate species mixing ratios after the 5-day simulations were then used for comparison with observations (Table III).

Several time-dependent NO_x simulations were also performed to assess how quickly the mixing ratio of intermediate species (H_2O_2 and CH_3OOH) responded to model decays in NO_x (Figures 2 and 3). In these simulations, NO_x was calculated along with CH_2O, H_2O_2, CH_3OOH while other longer-lived species were constrained (O_3, CO, H_2O, VOCs, PANs, HNO_3). The goal of these simulations was to assess whether these intermediate species maintain steady-state for conditions in the arctic free troposphere.

24-hr average O_x production and loss rates were calculated from the model output at diel steady-state (Figures 5 and 6). The model was defined to be at diel steady-state when radical species were repeating their diurnal cycles within 5%. All measured species were initialized in the model at their median values. NO_x was also held constant at its median measured value during these simulations, while NO and NO_2 were calculated. The mixing ratio of measured intermediate species (CH_2O, CH_3CHO, H_2O_2, CH_3OOH, PAN, PPN, HNO_3) were also constrained at their observed medians. Measured CH_3CHO mixing ratios were highly uncertain, mainly due to issues involved in sampling oxygenated hydrocarbons. As a result, measured CH_3CHO mixing ratios should be considered as estimates (D. Blake,

Table III. Model results for intermediate species after the 5th day for a series of constrained simulations

58–85° N	5th day mixing ratios	February (pptv)	March (pptv)	April (pptv)	May (pptv)
3–6 km	CH_2O	29	49 SS	39 SS	64 SS
	H_2O_2	128	238	309	445
	CH_3OOH	66	109 SS	104 SS	119 SS
1–3 km	CH_2O	33	49 SS	52 SS	111 SS
	H_2O_2	99	248	611	895
	CH_3OOH	87	140 SS	207 SS	268 SS

Simulations constrained at median measured NO_x, O_3, CO, H_2O, HCs, acetaldehyde, methanol, acetone, PAN, PPN, HNO_3, CH_2O, CH_3OOH, H_2O_2. The species of interest for a simulation (CH_2O, H_2O_2 or CH_3OOH) were calculated for that simulation. SS indicates the species reached steady-state.

personal communication). However, in comparing the observed free tropospheric CH_3CHO mixing ratios in Tables I and II with other *in situ* measurements (Singh, 2001), we find similar ranges, generally between 100–200 pptv for the free troposphere. Simulations were also performed with calculated CH_3CHO; however, the assumption of constrained versus calculated CH_3CHO had a negligible impact on the O_x photochemical production and loss rates.

3. Results and Discussion

3.1. MODEL EVALUATION: RADICAL SPECIES AND THEIR DEPENDENCE ON O_3 PHOTOLYSIS FREQUENCY

To evaluate how well the model constrained by medians represents the variability in observations, we compare the dependence of free radical species concentrations on the measured photolysis frequency, $j(O^1D)$. Free radical species and families, such as OH and $RO_x \equiv (HO_x + CH_3O_x +$ higher analogs), have lifetimes on the order of seconds to minutes, and thus should be in chemical steady-state. As a result, their concentrations will adjust rapidly to local photolysis frequencies. Figure 1(a) compares the model and measurement dependence of log(OH) on $\log(jO^1D)$ for March and May observations between 1–3 km and 58–85° N. Figure 1b compares the model and measurement dependence of $\log(RO_x)$ on $\log(jO^1D)$ for February and May conditions between 3–6 km and 58–85° N. Here, modeled $j(O^1D)$ was calculated from TUV and measured $j(O^1D)$ taken from the aircraft observations. The solid points and vertical bars represent the mean and 1σ limits for data points binned into $\log(jO^1D) = 0.25$ intervals. The variability in observations is due to a combination of measurement imprecision and atmospheric sampling variability. The estimated uncertainties (2σ) in the OH and RO_x measurements are $\pm 46\%$

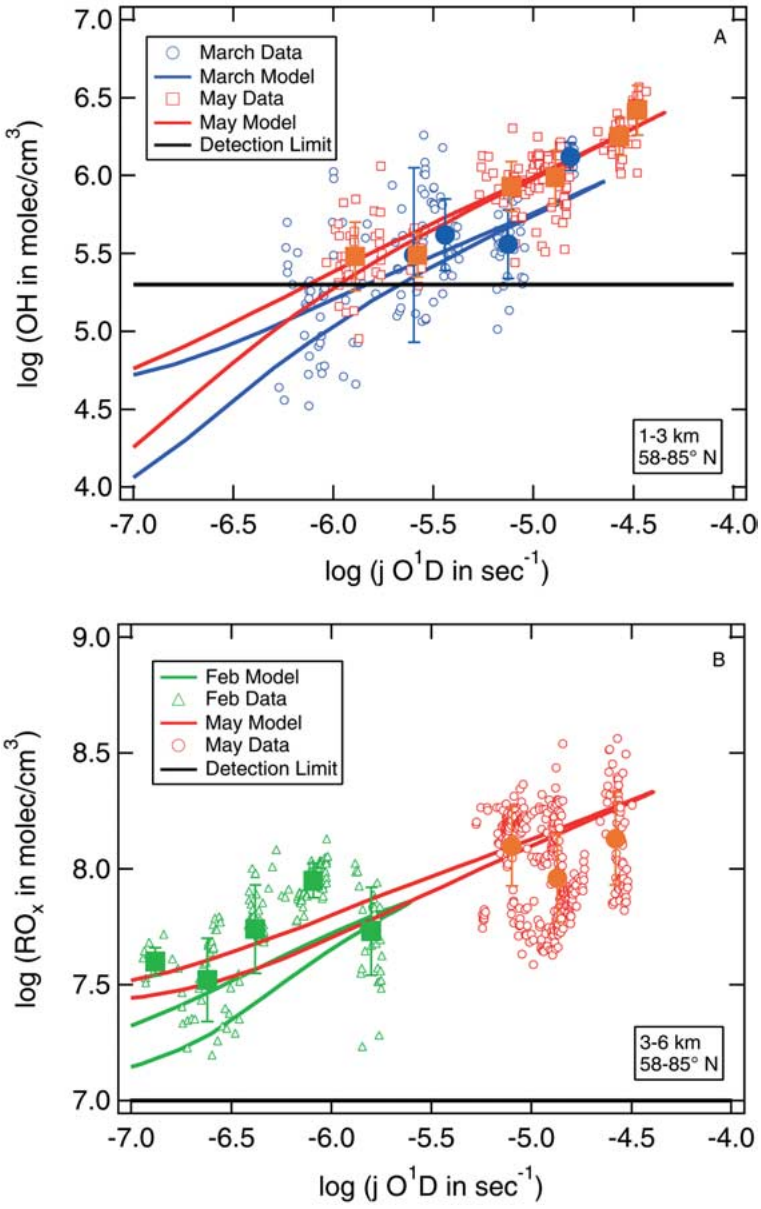

Figure 1. Dependence of radical concentration (OH in panel a and RO_x in panel b) against O_3 photolysis frequency. Open points are individual measurements and solid points are binned averages with one standard deviation limits. Points are separated by month and altitude for the 58–85° N latitude band. OH measurements were not available for February. The curves are modeled radical concentrations vs. modeled TUV $j(O^1D)$ for a diurnal cycle at diel steady-state. TUV parameters were set at 58° N and the end of month to expand modeled TUV $j(O^1D)$ so as to span all the individual points. Simulations constrained at median measured NO_x, O_3, CO, H_2O, HCs, acetaldehyde, methanol, acetone, PAN, PPN, HNO_3, CH_2O, CH_3OOH and H_2O_2.

(LOD = 2×10^5 molec/cm^3) and ±35% (LOD = 1×10^7 molec/cm^3), respectively. There was also evidence for atmospheric sampling variability in the radicals due to short-term changes in NO_x. Although the large variability in the observations does not provide a stringent test, it is encouraging that the box model, initialized with median observations for long-lived species, does yield modeled curves that generally reproduce the measured radical concentration dependence on $j(O^1D)$, within the 1σ limits. This lends confidence in the box model and in its usefulness in representing the local chemistry for the various regimes observed during TOPSE.

Figure 1 also illustrates the springtime increase in photochemical activity. Measurements acquired during May have both the highest $j(O^1D)$ frequencies and radical concentrations observed in the arctic free troposphere. This seasonal increase in RO_2 concentration is similar to the seasonal trend observed by Zanis *et al.* (2003) for a mountain site in the Swiss Alps. The average observed OH and RO_x concentrations for the largest $j(O^1D)$ bin in May were 2.5×10^6 and 1.4×10^8 molec/cm^3, respectively. This compares with modeled OH and RO_x concentrations of 2.0×10^6 and 1.8×10^8 molec/cm^3 for the same $j(O^1D)$ levels, respectively. The modeled curves and measurements in Figure 1(b) have a slope of ~1/2, which stems from the loss rate of RO_2 and its quadratic dependence on RO_2 concentration. Figure 1 also illustrates the asymmetry in the modeled radical diurnal profiles, which stems from the relatively long lifetime of the HNO_4 reservoir. In the model, HNO_4 builds in mixing ratio during the day and then slowly decays throughout the night. As a result, HNO_4 acts as a sink for radicals in the morning and a source of radicals in the evening.

3.2. MODEL EVALUATION: NON-RADICAL SPECIES AND THE STEADY-STATE ASSUMPTION

To further validate our understanding of the photochemistry in the model and test the steady-state assumption for non-radical species, we made model-measurement comparisons for longer-lived intermediate species (H_2O_2, CH_3OOH and CH_2O). As outlined in the model methodology, we performed model simulations individually for CH_2O, H_2O_2 and CH_3OOH to derive time-dependent mixing ratios for each intermediate, i.e., all measured species constrained at medians except for the species of interest, which was initialized at its median mixing ratio and calculated. If the photochemical box model was run for extended periods of time (60 and 10 days for February and May conditions, respectively), these model simulations generated steady-state concentrations for the intermediate species (H_2O_2 was limiting). Table III lists the mixing ratios after five-day simulations. Species that reached steady-state in the model after 5 days are denoted with 'SS'. In comparing these results with the measured medians in Tables I and II, we see that the general agreement between these intermediates improves when the species are denoted in diel steady-state. Our box modeling approach constrained with observed medians does not capture the atmospheric variability in observations. Given the large variabil-

ity in observed CH_2O throughout the campaign, our modeling approach did not enable a definitive CH_2O comparison. We refer the reader to Fried *et al.* (2003) for a detailed description of a point box model comparison with individual CH_2O observations. However, in looking at the peroxide mean mixing ratios and 1σ standard deviations in Tables I and II, the variabilities in the means decreases with season enabling a comparison between our modeling approach and the peroxide observations for April and May conditions. The simulations used to generate the modeled data in Table III illustrate that H_2O_2 has a time constant greater than 5 days to reach steady-state, while CH_3OOH reached steady-state in the model for all months except February. The lifetimes of H_2O_2 and CH_3OOH under February conditions (considering photolysis and reaction with OH) were calculated to be 15 days and 9 days, respectively. Atmospheric lifetimes will likely be shorter for the peroxides due to the additional heterogeneous loss mechanism, especially for the more water-soluble H_2O_2. Table III shows that modeled steady-state CH_3OOH mixing ratios are very similar to the measured medians for all months. H_2O_2 does not reach steady-state after 5 days, even in May, and as shown in Table III, its 5-day modeled mixing ratio in May is considerably higher than the measured H_2O_2 median by a factor of 2.6. In fact, while both the model and observations show a seasonal increase, the ratio of model-to-measurement does not show a significant change, even though the H_2O_2 lifetime decreases to 2.3 days.

Further simulations were performed to test the sensitivity of peroxides to NO_x mixing ratios. Model H_2O_2 was shown to be largely insensitive to small changes in NO_x about the median, $d\ln[H_2O_2]/d\ln[NO_x] = 0.035$ (February, 3–6 km), while CH_3OOH did show a significant negative sensitivity toward NO_x, $d\ln[CH_3OOH]/d\ln[NO_x] = -0.31$. Additional time-dependent NO_x simulations were also used to assess how the peroxide mixing ratios changed as NO_x decreased over a 3-day period to the median measured NO_x. Figure 2 illustrates the time-dependent NO_x simulations for May conditions, respectively. H_2O_2 showed a consistent increase during the simulation with H_2O_2 not reaching steady-state during the 6-day window. CH_3OOH initially decreased during the simulation consistent with the higher NO_x mixing ratios and the negative CH_3OOH sensitivity towards NO_x; however, it then increased for the remainder of the simulation. At $t =$ 3 days, modeled H_2O_2 is already considerably higher than the measured median, while CH_3OOH is consistent with the measured median. In comparing H_2O_2 and CH_3OOH, the H_2O_2 medians are likely impacted by heterogeneous loss to a greater extent than CH_3OOH. Thus, H_2O_2 is likely initialized considerably lower than our model steady-state value (no heterogeneous loss for peroxides in box model) in comparison to CH_3OOH. The long lifetime for the peroxides results in the modeled H_2O_2 not approaching its modeled steady-state during the 6-day window. In the arctic free troposphere, after a heterogeneous loss process, there is a long time constant for H_2O_2 re-approaching steady-state with its longer-lived precursor species. This slow time constant hinders quantitative H_2O_2 model-measurement comparisons with a box model. However, while the intermittent nature of cloud encounter

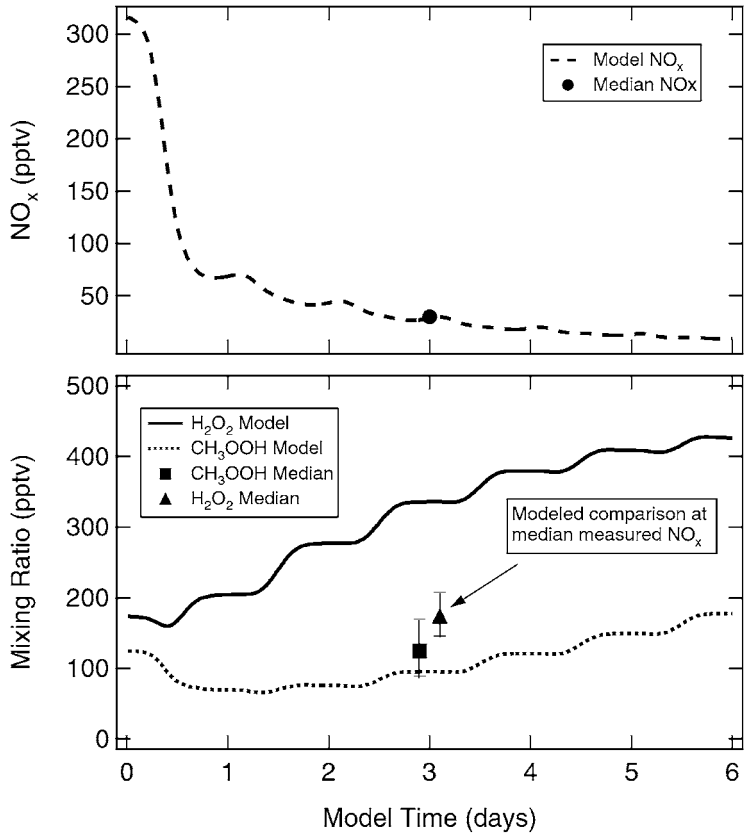

Figure 2. Model-measurement comparison of peroxide species for May conditions. The points are median measured mixing ratios for CH_3OOH and H_2O_2 and are plotted at $t = 0$. Model curves represent results from a time-dependent NO_x simulation where NO_x was initialized higher and decreased over a three day initiation time to its median measured mixing ratio of 30 pptv at $t = 0$. Vertical bars are the 25 and 75 percentiles. Simulations constrained at median measured O_3, CO, H_2O, HCs, acetaldehyde, methanol, acetone, PAN, PPN and HNO_3.

and heterogeneous loss may explain episodic model-measurement differences, it does not seem likely that, in an average sense, H_2O_2 measurements over a wide area in the 3–6 km layer would be affected by heterogeneous loss by a factor more than 2. Uncertainties raised here in modeling H_2O_2 will need to be considered later in discussing the RO_x and O_x budget.

3.3. CHARACTERISTICS OF RADICAL POOL CYCLING

Radical species are produced, lost and inter-converted by numerous chemical channels. It is instructive to calculate diurnally averaged fluxes for critical reaction pathways with a photochemical model. Figure 3 illustrates the behavior of the

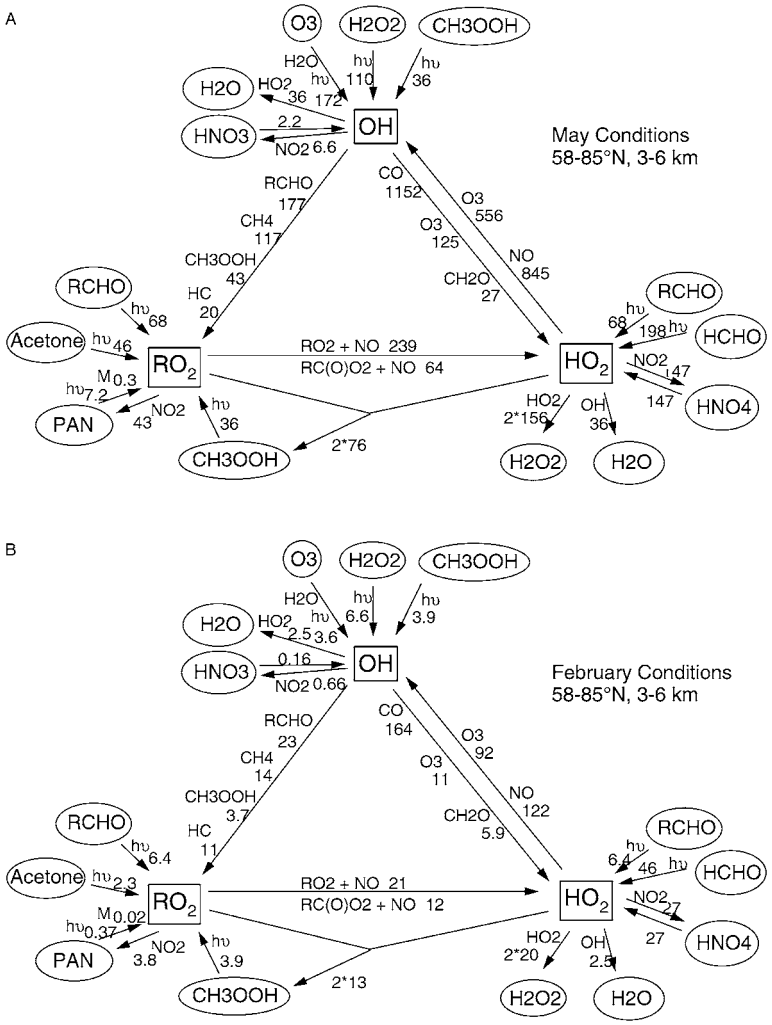

Figure 3. Radical pool cycling for May (panel a) and February (panel b) condition in the arctic free troposphere (58–85° N and 3–6 km). Numbers are model-derived diurnally averaged fluxes in pptv/day. Simulations constrained at median measured NO_x, O_3, CO, H_2O, HCs, acetaldehyde, methanol, acetone, PAN, PPN, HNO_3, CH_2O, CH_3OOH and H_2O_2.

radical pool for May (panel a) and February conditions (panel b) in the arctic free troposphere. Diurnally averaged radical production rates in pptv/day are labeled for so-called primary photolysis reactions (O_3), secondary photolysis reactions (RCHO, H_2O_2, CH_3OOH and $CH_3C(O)CH_3$) and inter-conversion reactions. Several features in Figure 3 are prominent in importance due to the measurement location in the remote arctic free troposphere. OH is lost predominantly by reaction with CO for both May and February conditions. While the hydrocarbon reactions with OH have their greatest importance in winter, they still only contribute 5% to

OH loss in February while CO contributes 70%. The second largest contributor to OH loss is the sum of the aldehyde species (CH_2O and CH_3CHO were constrained at measured medians while other aldehydes were calculated from higher hydrocarbon chemistry in the model). H_2O and HNO_3 formation are terminal sinks for OH. H_2O formation dominated over HNO_3 formation in this low NO_x environment. The result is an overall OH loss rate of 43 pptv/day (May) and 3.2 pptv/day (February); compared with an OH to peroxy radical conversion rate of 1660 pptv/day (May) and 233 pptv/day (February). This implies that for every OH radical that is terminated, 39 (May) and 73 (February) are inter-converted to the peroxy radical pool. The OH production also proceeds through recycling reactions from HO_2. It is interesting that in the arctic free troposphere, the reaction of HO_2 with O_3 is comparable (556 pptv/day in May and 92 pptv/day in February) to the reaction between HO_2 and NO (845 pptv/day in May and 122 pptv/day in February) in recycling OH. The primary source of OH from O_3 photolysis in February is very small (3.6 pptv/day). This is only 1.7% of the OH regeneration rate from HO_2. Furthermore, the photolysis of peroxides to produce OH is a factor of 2.9 times larger than O_3 photolysis in February. The differing sensitivities of peroxide photolysis and O_3 photolysis on the low wintertime water vapor mixing ratios contributes to the importance of peroxide photolysis in winter. While both the peroxide photolysis rate and the $O(^1D) + H_2O$ reaction rate increase with water vapor, a further simulation with water vapor an order of magnitude larger for February conditions resulted in a factor of 11.5 increase in OH production from O_3 photolysis and a factor of 2.7 increase from H_2O_2 photolysis. This change in water vapor resulted in OH production now having a larger contribution from O_3 photolysis (42 pptv/day) compared to H_2O_2 photolysis (18 pptv/day). In May, the O_3 photolysis contribution to OH formation is larger than peroxide photolysis; however, both terms are comparable. In May, the O_3 and peroxide photolysis sources of OH are 12% and 10%, respectively, of the regeneration rate from HO_2. The model runs used in Figure 3 were performed with H_2O_2 constrained to observed medians. Results with H_2O_2 calculated by the model yield even larger estimates for H_2O_2 photolysis and OH production suggesting that our uncertainty in H_2O_2 translates into an uncertainty in understanding the OH budget.

The sources and cycling of the peroxy radical pool are highly complex, even in a remote environment. RO_2 can be regenerated from OH recycling reactions. Secondary sources include the photolysis of intermediate VOC oxidation products such as aldehydes, ketones and peroxides. In looking at the sources to the total radical pool, the magnitude of the RO_2 photolysis sources are comparable with the OH photolysis sources in May (416 pptv/day vs. 318 pptv/day); however, in February, RO_2 photolysis sources dominate over OH photolysis sources (65 pptv/day vs. 14 pptv/day). Furthermore, an organic peroxy radical can react with NO via a complex series of intermediate steps involving alkoxy radical decomposition, O_2 abstraction or isomerization to form an HO_2 radical. As noted above, peroxy radicals can cycle back to OH by reactions with NO and O_3; however for low

NO_x environments, peroxy radicals can also enter self-reactions forming peroxides. Under May conditions, HO_2 is converted back to OH at a rate of 1400 pptv/day. This can be compared to an HO_2 self reaction loss equal to 312 pptv/day, an HO_2 + CH_3O_2 reaction rate equal to 76 pptv/day and a HO_2 + OH reaction equal to 36 pptv/day. Thus, for every HO_2 radical that is terminated to form a peroxide or H_2O, 3.0 are recycled back to OH. In February, this estimate changes only slightly with 3.7 HO_2 radicals recycled back to OH for every HO_2 terminated. This is in contrast to regions impacted by fresh emissions of NO_x (VOC/NO_x $<$ 10) where the rate of the HO_2 self-reaction is small compared to the rate of chain propagation by reaction of HO_2 with NO (Seinfeld and Pandis, 1998).

It should be further emphasized that our uncertainty in modeling H_2O_2 translates to an uncertainty in the RO_x budget. For example, the model overestimate of H_2O_2 could imply a model overestimate of RO_x radical loss. Given the quadratic dependence of H_2O_2 formation on HO_2 mixing ratios, a modeled steady-state H_2O_2 over-prediction by a factor of 3.6 for May conditions (from a 10 day simulation) could imply that modeled HO_2 is being over-predicted by a factor of 1.9. However, these implications assume that steady-state is a reasonable assumption for H_2O_2 in May and that H_2O_2 loss is dominated by OH oxidation and photolysis, both of which are not strictly valid at all times in the springtime arctic free troposphere. Thus, our difficulty in modeling H_2O_2 adds uncertainty in our quantification of the RO_x budget.

A parameter useful in understanding how the radical cycling in the arctic free troposphere varies with NO_x and P_{RO_x} (P_{RO_x} is defined here as the total production rate of RO_x considering O_3, CH_2O, H_2O_2 and CH_3OOH photolysis) is the radical chain length, defined here as the production rate of OH through recycling reactions divided by the total loss rate of all radical species. Physically, the radical chain length represents the number of times an OH radical is recycled within the RO_x family before being terminated. Figure 4 illustrates the dependence of the radical chain length on NO_x, color-coded by P_{RO_x}. Individual points are calculated by combining observations for NO_x, RO_x, O_3, CH_2O, H_2O, j values, H_2O_2, CH_3OOH with the point steady-state calculations Cantrell *et al*. (2003) used for the partitioning between the RO_x family. Curves were calculated from the photochemical box model as a function of varying NO_x. The individual points and modeled calculations lie between 0.2–6 with the points showing considerable scatter compared to the model. Points are binned for NO_x in the range 10–30 pptv and 30–50 pptv and P_{RO_x} between 0–200 pptv/day, 600–1000 pptv/day, and 1300–1800 pptv/day. The binning considerably reduces the scatter as the model now generally lies within the 1σ data limits, although comparing any modeled trend with the observations is beyond the measurement precision. In looking at the modeled dependence, intriguing relationships are observed for the range of NO_x and P_{RO_x} observed in the arctic free troposphere. At low P_{RO_x}, the modeled radical chain length decreases with increasing NO_x. This is the case for February conditions as radical concentrations are low, radical-radical reactions are slow and RO_x + NO_x reactions (PAN, HNO_4 and

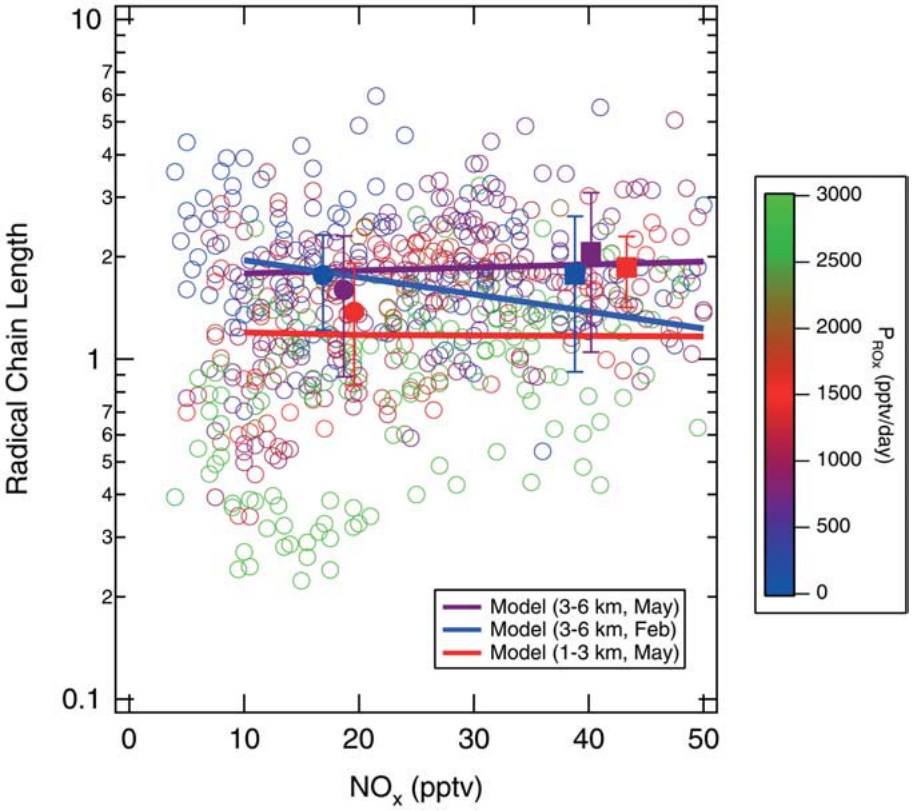

Figure 4. Dependence of radical chain length on NO_x and P_{RO_x}. Chain length is defined as the recycling production rate of OH (reaction 1 + reaction 6) divided by the total loss of RO_x. Points are calculated from measurements of NO, NO_2, RO_x, O_3, H_2O, CH_2O, H_2O_2, CH_3OOH, $j(O^1D)$ and steady-state calculations of OH, $CH_3C(O)O_2$ and the partitioning of RO_x between HO_2 and CH_3O_2 [Cantrell *et al.*, 2003]. Data is binned based on NO_x between 10–30, 30–60 pptv for P_{RO_x} in the ranges 0–200, 600–1000, 1300–1800 pptv/day. Curves are model-derived results for various cases, color-coded against model calculated P_{RO_x}. Simulations constrained at median measured O_3, CO, H_2O, HCs, acetaldehyde, methanol, acetone, PAN, PPN, HNO_3, CH_2O, CH_3OOH, H_2O_2 with varying NO_x.

HNO_3 formation) become important with only modest increases in NO_x mixing ratios. At higher P_{RO_x} representative of May conditions, modeled chain lengths are nearly independent of NO_x. The strongest dependence between chain length and P_{RO_x} is observed at low NO_x. Here, radical chain lengths increase with decreasing P_{RO_x} because RO_x sinks are quadratic in RO_x mixing ratios. At higher P_{RO_x} rates, the observed points clearly show chain length increasing with NO_x. Here, the increase in the chain length is driven by increases in the HO_2 + NO reaction with increasing NO_x. These observations (blue points in Figure 4) generally correspond to mid-latitude observations later in spring.

3.4. SEASONAL DEPENDENCE OF THE O_x PRODUCTION AND LOSS RATES

A key objective of TOPSE was to quantify the O_x budget during the observed springtime maximum in tropospheric O_3. For our sorted data set (1–3 km, 58–85° N), median O_3 was observed to increase by 12 ppbv between February and May. The increase was even larger at higher altitudes in the free troposphere with an observed median O_3 increase of 24 ppbv between February and May (3–6 km and 58–85° N). Assessing the importance of the various source terms for O_3 is difficult with a 0-D photochemical box model. O_3 has a long lifetime; for TOPSE conditions, generally ranging between 10–100 days. As a result, transport in addition to chemistry can significantly impact measured O_3 mixing ratios. To assess the importance of the *in situ* O_3 production relative to transport for air masses in the arctic free troposphere, we used the box model to estimate gross O_x production and loss rates for our defined regimes. Figure 5 presents the seasonal dependence in the diurnally-averaged gross O_x production rate, P_{O_x}, calculated with the box model constrained with data medians from 58–85° N and 1–3 km (panel a) and 3–6 km (panel b). P_{O_x} is divided into source terms from HO_2, organic peroxy radical ($R'O_2$) and organic peroxyacyl radical ($R'C(O)OO$) reactions with NO,

$$HO_2 + NO \rightarrow OH + NO_2 \tag{R1}$$

$$R'O_2 + NO \rightarrow R'O + NO_2 \tag{R2}$$

$$R'C(O)OO + NO \rightarrow R' + CO_2 + NO_2 \tag{R3}$$

$$NO_2 + h\nu \rightarrow NO + O \tag{R4}$$

$$O + O_2 + M \rightarrow O_3 + M \tag{R5}$$

where reactions (1–3) are the rate-limiting steps in O_3 production. These two panels illustrate the strong seasonal increase in local O_x production in the arctic free troposphere. The increase in O_x production rates is driven, in large part, by a combination of increases in instantaneous actinic flux, integrated exposure to actinic flux (a unique feature of the high latitude winter-to-spring transition), RO_x precursor compounds (water vapor, O_3, peroxides, aldehydes), and NO_x. The reader is referred to Cantrell *et al.* (2003) for a detailed description of the peroxy radical budget and the relative importance of various precursor species throughout the springtime transition. Reaction (1) dominates over reactions (2–3) contributing between 66% (February, 1–3 km) and 69% (May, 1–3 km) to the gross O_x production; note the importance of reaction (1) increases relative to reactions (2–3) with season. The slower rate of increase in O_x production between March and April in the 3–6 km band stems from lower median water vapor and NO_x in April compared to March. The modeled seasonal O_x production rate increases more sharply in the lower free troposphere (a factor of 28 for 1–3 km between February and May) compared to the middle free troposphere (a factor of 7 for 3–6 km between February

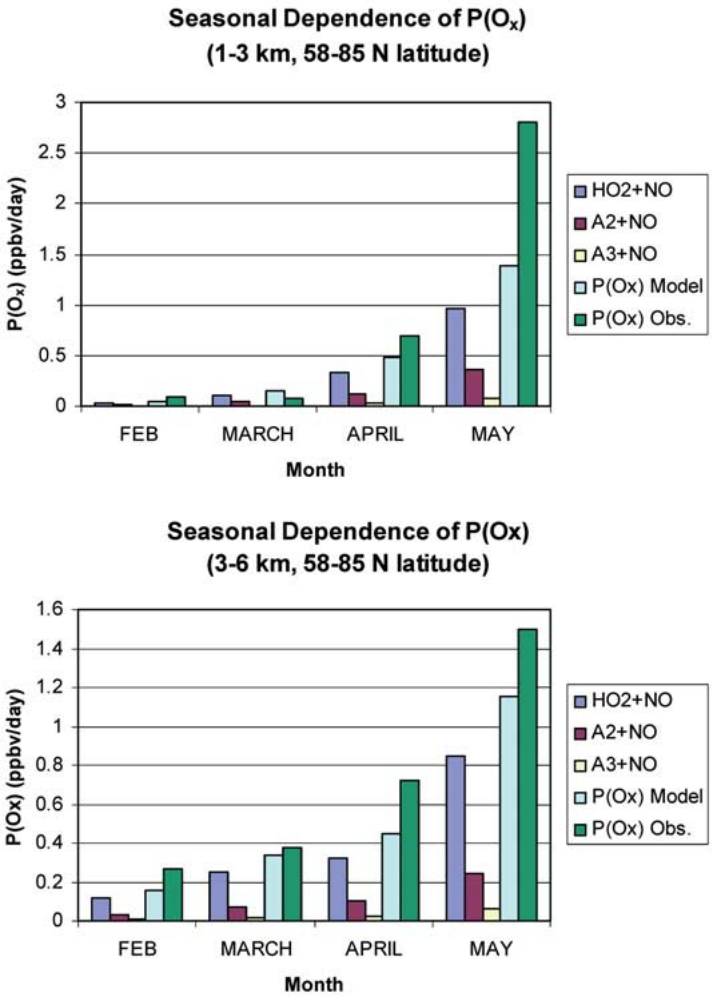

Figure 5. Comparison of the seasonal dependence of the gross O_3 production rate (ppbv/day) between 3–6 km (panel a) and 1–3 km (panel b) for 58–85° N derived from both the model (run on medians) and observationally (using coincident RO_2 and NO observations). Rates are divided between contributions from HO_2, $R'O_2$ and $R'C(O)O_2$. Simulations constrained at median measured NO_x, O_3, CO, H_2O, HCs, acetaldehyde, methanol, acetone, PAN, PPN, HNO_3, CH_2O, CH_3OOH and H_2O_2.

and May). This largely stems from a sharper increase in median NO_x mixing ratios in the lower free troposphere (7–27 pptv) compared to the mid troposphere (18–30 pptv). Also included in Figure 5 is the P_{O_x} derived solely from observed RO_2 mixing ratios and observed NO mixing ratios, $k[RO_2][NO]$, where k is approximated by the HO_2 + NO rate coefficient. While the observation-derived P_{O_x} is generally higher than the model-derived P_{O_x} (at most by a factor of 2), a similar seasonal dependence is noted for both altitude bands.

Table IV. Diurnally-averaged gross O_x production rates calculated from prior field campaigns

	STRAT [a]	SUCCESS [a]	SONEX [a]	TRACE A [b]	FREETEX96 [c]
	21–38° N	36–40° N	39–54° N	20° N–40° S	Swiss Alps
	all year	April–May	Oct.–Nov.	Sept.–Oct.	April–May
	8–12 km	8–12 km	8–12 km	0–12 km	3.6 km
	0.85	2.3	0.54	8.0 (0–4 km)	
$P(O_x)$				3.8 (4–8 km)	7.7
(ppbv/day)	(0.6–1.1)	(0.97–5)	(0.35–0.8)	2.9 (8–12 km)	

[a] Median values and ranges (in parentheses) are tabulated. Data compiled in Jaegle *et al.* (2001).
[b] Median values are tabulated in three altitude ranges. Data from Jacob *et al.* (1996).
[c] Mean values for daytime conditions (08:00–20:00 UTC). Data from Zanis *et al*. (2000).

The gross O_x production rates in the arctic free troposphere during TOPSE can be compared with rates from other recent missions over northern mid to high latitudes such as STRAT (Stratospheric Tracers for Atmospheric Transport), SUCCESS (Subsonic Aircraft: Contrail and Cloud Effects Special Study), SONEX (Subsonic Assessment: Ozone and Nitrogen Oxide experiment) and FREETEX (Free Tropospheric Experiment). The common feature among these other missions was an altitude range in the free troposphere. The STRAT mission took place over the North Pacific between California and Hawaii in three seasonal deployments (October–November, January–February and August). The SUCCESS mission took place over the central United States from April to May. The SONEX campaign took place over the North Atlantic region between October and November. FREETEX/96 resided on a mountain site in the Swiss Alps from April 15 to May 24, 1996. An additional study, TRACE A, had measurements throughout the troposphere but focused on the region in the South Atlantic east of Brazil in September and October. Table IV compiles the gross O_x production rates calculated for these missions and can be compared to the results in Figure 5 for TOPSE. The initial deployments during TOPSE yield some of the lowest gross O_x production rates reported in the troposphere ($<$0.2 ppbv/day for February, 58–85° N). The timing of the SONEX campaign in late fall coincides with similar actinic fluxes for the early spring during TOPSE; however, direct comparison should be made with TOPSE conditions in the 40–50° N band to coincide with the 39–54° N latitude band during SUCCESS. A box model simulation for median conditions in February between 3–6 km and 40–50° N resulted in a P_{O_x} of 0.43 ppbv/day, similar to the 0.54 ppbv/day median P_{O_x} observed during SONEX (Jaegle *et al*., 2000).

Figure 6 presents the seasonal dependence in the diurnally averaged production, loss and net production of O_x in the arctic free troposphere. The results were generated from our box model constrained with median data between 58–85° N and for 1–3 km (panel a) and 3–6 km (panel b). Figure 6 also includes results from two

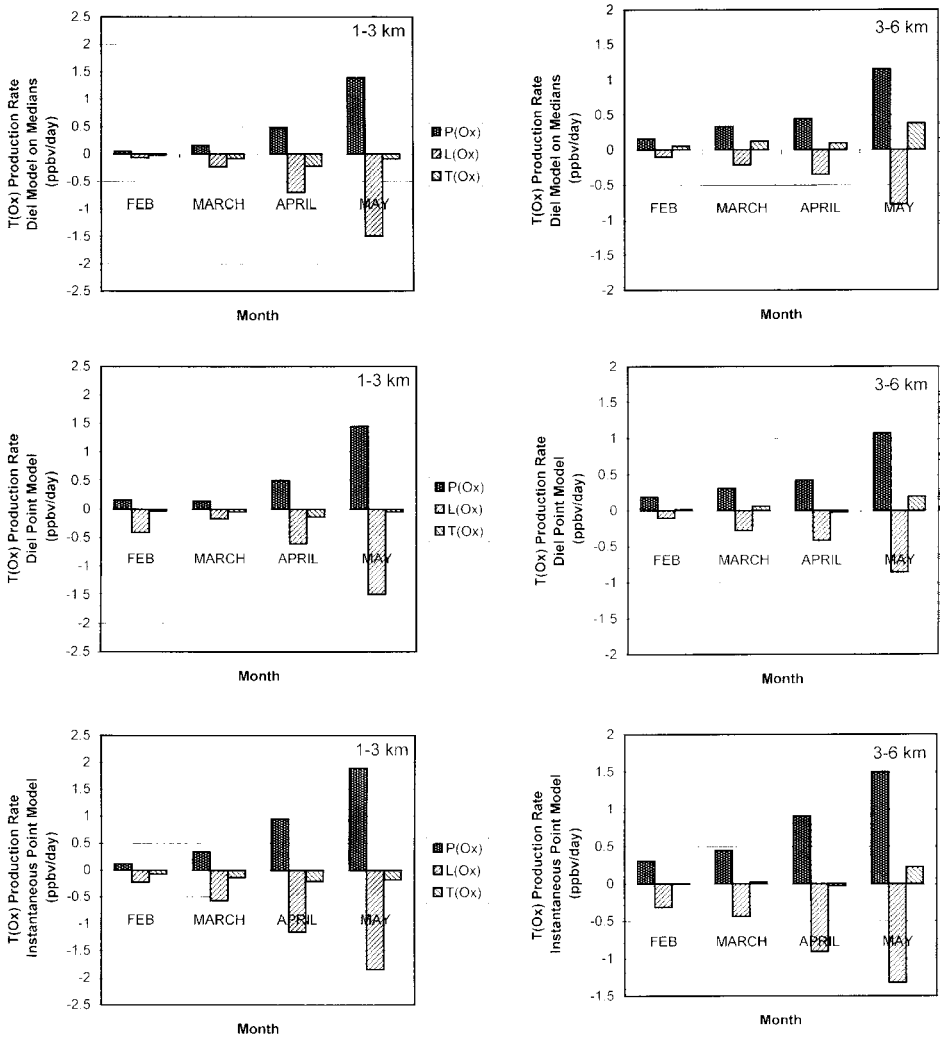

Figure 6. Comparison of the seasonal dependence of net O_3 production rate (ppbv/day) between 3–6 km (panel a) and 1–3 km (panel b) for 58–85° N with two other box modeling approaches (Wang *et al.*, 2003; Cantrell *et al.*, 2003). Our simulations were constrained at median measured NO_x, O_3, CO, H_2O, HCs, acetaldehyde, methanol, acetone, PAN, PPN, HNO_3, CH_2O, CH_3OOH and H_2O_2.

point box models (Wang *et al.*, 2003; Cantrell *et al.*, 2003). The Wang *et al.* model was run to diel steady-state for each data point. The Cantrell *et al.* model was run to instantaneous steady-state using the observed j values for each data point. For both point models, O_3 rates from individual points were calculated, divided into the latitude, altitude and month bins in Tables I and II and then sorted to calculate the median P_{O_x}, L_{O_x} and T_{O_x}. This differs form our modeling approach of constraining a box model based on the observed medians, integrating it for 5 days to diel steady-

state and then calculating rates for P_{O_x}, L_{O_x} and T_{O_x}. While our approach is similar to the Wang *et al.* model in that it calculates diurnally averaged rates, our model has the advantage of using a more explicit organic oxidation scheme while having the disadvantage of not being automated to run on individual points and thus cannot capture atmospheric variability. The three model approaches do provide a unique opportunity to compare the importance of the various assumptions in the models. Interestingly, all three models yield a consistent picture for the local O_x photochemical rates in the arctic free troposphere. This suggests that the detailed organic chemistry in our box model is not critical to deriving O_x rates for the remote arctic free troposphere and that atmospheric conditions are uniform enough for a box model constrained by median observations to capture the seasonal trends in the O_x budget. Generally, the mid-troposphere shows a tendency for net O_x production throughout the mission while the 1–3 km layer shows a small tendency for net loss of O_3. This combined with the generally increasing O_3 mixing ratio throughout the campaign directly imply the necessity for a net import of O_3 transported into the arctic lower free troposphere.

Our uncertainty in modeling H_2O_2 also adds uncertainty to the model-derived O_x photochemical rates. To evaluate the sensitivity of the O_x budget to our uncertainty in H_2O_2, we calculated P_{O_x}, L_{O_x} and T_{O_x} from a series of simulations where H_2O_2 was allowed to reach diel steady-state. For February conditions, this resulted in a 23% increase in P_{O_x} and a 22% increase in T_{O_x} compared to the simulations with H_2O_2 constrained by observations. For May conditions, this resulted in a 16% increase in P_{O_x} and a 10% increase in T_{O_x}.

It would be advantageous to apply a simple method to estimate the relative importance of transport and local photochemical production to the observed O_3 mixing ratios during TOPSE. The local derivative of O_x with respect to time can be expressed in terms of the local O_x production rate (P_{O_x}), the local O_x loss rate (L_{O_x}) and a term representing transport of O_3 into the arctic free troposphere (T):

$$\frac{d[O_x]}{dt} = P_{O_x} - L_{O_x}[O_x] + T. \tag{2}$$

Solution of Equation (2) leads to the following expression for O_x (Klonecki and Levy, 1997; Cantrell *et al.*, 2003):

$$[O_x]_t = [O_x]_{ss} + ([O_x]_o - [O_x]_{ss}) \exp(-L_{O_x} t), \tag{3}$$

where $[O_x]_{ss}$ is the steady-state O_x concentration equal to $(P_{O_x} + T)/L_{O_x}$. An implicit assumption in using Equation (3) is that $[O_x]$ changes are small so that P_{O_x} and L_{O_x} remain reasonably constant. The transport term, T, can be calculated by substituting the expression for $[O_x]_{ss}$ and rearranging Equation (3):

$$T = \frac{L_{O_x}[O_x] - P_{O_x} - L[O_x]_o \exp(-L_{O_x} t) + P_{O_x} \exp(-L_{O_x} t)}{1 - \exp(-L_{O_x} t)}. \tag{4}$$

Here, we compare our photochemical box modeled results run on median data with the point steady-state model (Cantrell *et al.*, 2003) and a 3-D chemical-transport

model (Emmons *et al*., 2002) to see if similar answers to this important question are observed with various modeling approaches. From our modeled estimates of P_{O_x} and L_{O_x} for each month and the observed median O_3 mixing ratios and a time increment of 1 month, it is possible to estimate the magnitude of the transport term. A positive value for T indicates net O_3 transport into the arctic free troposphere while a negative term indicates net O_3 transport out of the arctic free troposphere. The analysis implicitly assumes that the P_{O_x} and L_{O_x} values derived from the model are representative of the monthly period. Table V summarizes the results for T for 1–3 km and 3–6 km between 58–85° N. In all cases, we calculate net transport of O_3 into the arctic free troposphere (positive values for T). Between February and March in the 1–3 km layer, transport of O_3 into the region dominates the local photochemical production (78% vs. 22%). After March, the transport term is a small percentage (<26%) of the local production term (>74%), as the effects of increased photochemical activity increase the local rates of O_x production significantly. In the 3–6 km layer, the local production term always dominates the transport term with the transport term contributing a maximum percentage of 31% between February and March. These results are qualitatively consistent with the regional O_x budget derived by a 3-D chemical-transport model (MOZART) for the vertically integrated, 60–90° N latitude band (Emmons *et al*., 2002). MOZART derived a $d[O_x]/dt$ for transport greater than O_x production (5 Tg/mon vs. 1 Tg/mon) between February and March. Later in the season between April and May, MOZART derived a transport term that was less than the O_x production (3 Tg/mon vs. 6 Tg/mon). The steady-state point model described in (Cantrell *et al*., 2003) also derived a net import of O_x into the arctic troposphere between 0.1–0.4 ppbv/day compared to local production rates of 0.7–0.9 ppbv/day, similar to the magnitudes shown in Table V. The steady-state point model also derived a net export of O_x from the 40–60° N latitude band of 2–3 ppbv/day compared to local production rates of 6–8 ppbv/day. These results are also consistent with Zanis et al. (2000) who suggest a photochemical origin for the springtime O_3 maximum at Jungfraujoch, Switzerland. Collectively, these studies suggest that in winter O_x transport and local photochemical production both play comparable roles in the observed O_3 trend while the photochemical bloom later in the campaign results in local photochemical production dominating transport. While the box modeled results can infer a magnitude and sign for the transport term, it cannot discern the source of the O_3 being transported into the arctic free troposphere, i.e., transport from stratosphere or transport from the industrialized boundary layer farther south. The reader is referred to the 3-D model study by Emmons *et al*. (2002) for a further breakdown of the transport term into vertical and horizontal components.

Table V. Calculated O_3 photochemical production term and transport term needed to reproduce the monthly changes in median O_3 (58–85° N)

	February to March period		March to April period		April to May period	
3–6 km						
P_{O_x} (ppbv/day)	0.25	(69%)	0.39	(87%)	0.80	(80%)
T (ppbv/day)	0.11	(31%)	0.057	(13%)	0.20	(20%)
1–3 km						
P_{O_x} (ppbv/day)	0.10	(22%)	0.32	(74%)	0.93	(76%)
T (ppbv/day)	0.35	(78%)	0.11	(26%)	0.29	(24%)

In parenthesis are shown the percentages of the total for each term.
Simulations constrained at median measured NO_x, O_3, CO, H_2O, HCs, acetaldehyde, methanol, acetone, PAN, PPN, HNO_3, CH_2O, CH_3OOH, H_2O_2.

3.5. SENSITIVITY OF O_x PRODUCTION AND LOSS RATES TO NO_x MIXING RATIOS AND RO_x PRODUCTION RATES

Since the local gross O_3 production rate in the arctic free troposphere plays a considerable role in the observed seasonal O_3 trend, especially later in the campaign, it is desirable to examine the factors that influence O_x production rates. Numerous prior studies have suggested that in the remote troposphere gross O_3 production increases linearly with NO_x mixing ratios (so called NO_x-limited regime). To determine the sensitivity of P_{O_x} to NO_x, we calculated $\mathrm{dln}(P_{O_x})/\mathrm{dln}(NO_x)$ for each regime by using the model-derived change in P_{O_x} for small changes in NO_x mixing ratios ($\pm 10\%$). We derived $\mathrm{dln}(P_{O_x})/\mathrm{dln}(NO_x)$ values between 0.86–1.02, generally independent of month in the arctic free troposphere. This means that a 1% increase in NO_x mixing ratios will correspond to a 0.86–1.02% increase in gross O_x production rates. This implies that gross O_x production rates are strongly dependent on NO_x mixing ratios (a value of unity would imply linearity) in the arctic free troposphere, as has been observed for other low NO_x environments around the world (Ridley *et al.*, 1992; Schultz *et al.*, 1999; Jaegle *et al.*, 2000; Kotchenruther *et al.*, 2001). Similarly, we derived $\mathrm{dln}(L_{O_x})/\mathrm{dln}(NO_x)$ values less than 0.2, independent of month in the arctic free troposphere. This suggests that the O_x loss rate is generally independent of small changes in $[NO_x]$. Together these results imply that the net O_x tendency will also be strongly sensitive to small changes in NO_x mixing ratios in the arctic free troposphere.

Numerous prior studies have shown that O_x production rates depend on NO_x in a non-linear manner over a wide range of NO_x mixing ratios. In Figure 7 are calculated gross O_x production rate points as a function of measured NO_x mixing ratios for the entire TOPSE mission. P_{O_x} was calculated using measured RO_x and NO mixing ratios. Point steady-state calculations (Cantrell *et al.*, 2003) were used to partition the measured RO_x into HO_2 and CH_3O_2 fractions. The data are also color-

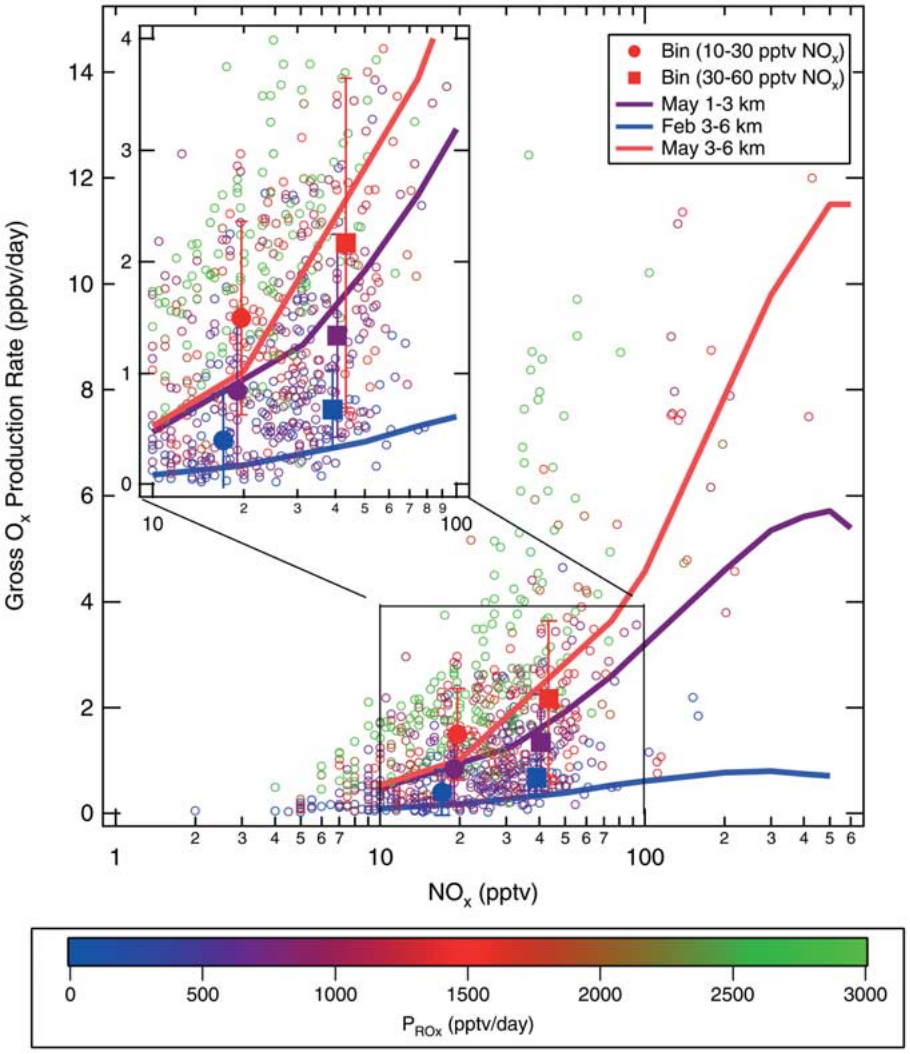

Figure 7. Dependence of gross O_3 production rate (ppbv/day) on NO_x, color-coded against P_{RO_x}. Points are calculated from measurements of NO, NO_x, RO_x, H_2O, O_3, CH_2O, H_2O_2, CH_3OOH, J_{O1D} and steady-state calculations of the partitioning of RO_x between HO_2 and CH_3O_2 [Cantrell *et al.*, 2003]. Data is binned based on NO_x between 10–30, 30–60 pptv for P_{RO_x} in the ranges 0–200, 600–1000, 1300–1800 pptv/day. Curves are model-derived results for various cases, color-coded against model calculated P_{RO_x}. Simulations constrained at median measured O_3, CO, H_2O, HCs, acetaldehyde, methanol, acetone, PAN, PPN, HNO_3, CH_2O, CH_3OOH, H_2O_2 with varying NO_x.

coded as a function of the RO_x production rate derived observationally considering O_3, CH_2O, H_2O_2 and CH_3OOH photolysis. Figure 7 clearly shows an increase in P_{O_x} with NO_x for a given RO_x production rate (linear for low NO_x). For a given NO_x mixing ratio, P_{O_x} also increases almost linearly with increasing P_{RO_x}. Also, included on Figure 7 are our photochemical model-derived curves corresponding to February (3–6 km) and May (1–3 km and 3–6 km) median conditions in the arctic free troposphere. Several model simulations were performed at constant RO_x precursor concentrations (P_{RO_x} = 85 pptv/day for February (3–6 km), 770 pptv/day for May (3–6 km) and 1500 pptv/day for May (1–3 km)) and different NO_x mixing ratios (spanning independent axis). The modeled lines are also color-coded based on the P_{RO_x} scale. The dependence of the modeled P_{O_x} curves on NO_x mixing ratios is very similar to that of the individual data points for comparable P_{RO_x} rates. The modeled curves are linear in P_{O_x} vs. NO_x at low NO_x; however, do appear to fall off at higher NO_x. Prior studies suggest that the optimum NO_x mixing ratio to maximize P_{O_x} decreases with lower P_{RO_x} rates. Jaegle *et al*. (2002) showed that for the upper troposphere, the optimum NO_x level is ~500 pptv for P_{RO_x} = 1000 pptv/day and decreases to ~200 pptv at P_{RO_x} = 10 pptv/day. Thornton *et al*. (2002) presented data for an urban, forested site during the 1999 Southern Oxidant Study (SOS) that showed P_{O_x} maximized at NO_x levels between 4–5 ppbv at P_{RO_x} as high as 60 ppbv/day. From our model simulations in the arctic free troposphere, P_{O_x} maximized at NO_x levels between 300 pptv (February, P_{RO_x} = 85 pptv/day) and 600 pptv (May, P_{RO_x} = 1500 pptv/day). These NO_x ranges are very similar in magnitude to the results obtained by (Jaegle *et al*., 2000) for comparable P_{RO_x} in the upper troposphere during STRAT, SUCCESS and SONEX. In comparing the modeled curves with the observations, it is not possible to discern curvature due to the majority of the data lying at low NO_x levels. The general agreement between the modeled curves and the observations lends further confidence in our understanding of the chemistry and its dependence on NO_x; however, the argument is somewhat circular as point steady-state calculations were used, in part, to calculate the P_{O_x} term. Furthermore, our assignment of P_{O_x} as the sum of the rates of peroxy radical reactions with NO also prescribes a predetermined understanding of what chemistry limits O_3 production.

Figure 8 illustrates how the net O_3 production rate depends on NO_x mixing ratios. Net O_3 production rates were calculated considering the following O_x loss reactions:

$$O_3 + HO_2 \rightarrow OH + 2O_2 \tag{R6}$$

$$O(^1D) + H_2O \rightarrow 2OH \tag{R7}$$

$$O_3 + OH \rightarrow HO_2 + O_2\,. \tag{R8}$$

Individual points were calculated from observations of RO_x, NO, O_3, J_{O1D}, and H_2O. Steady-state calculations (Cantrell *et al*., 2003) were used for OH and to

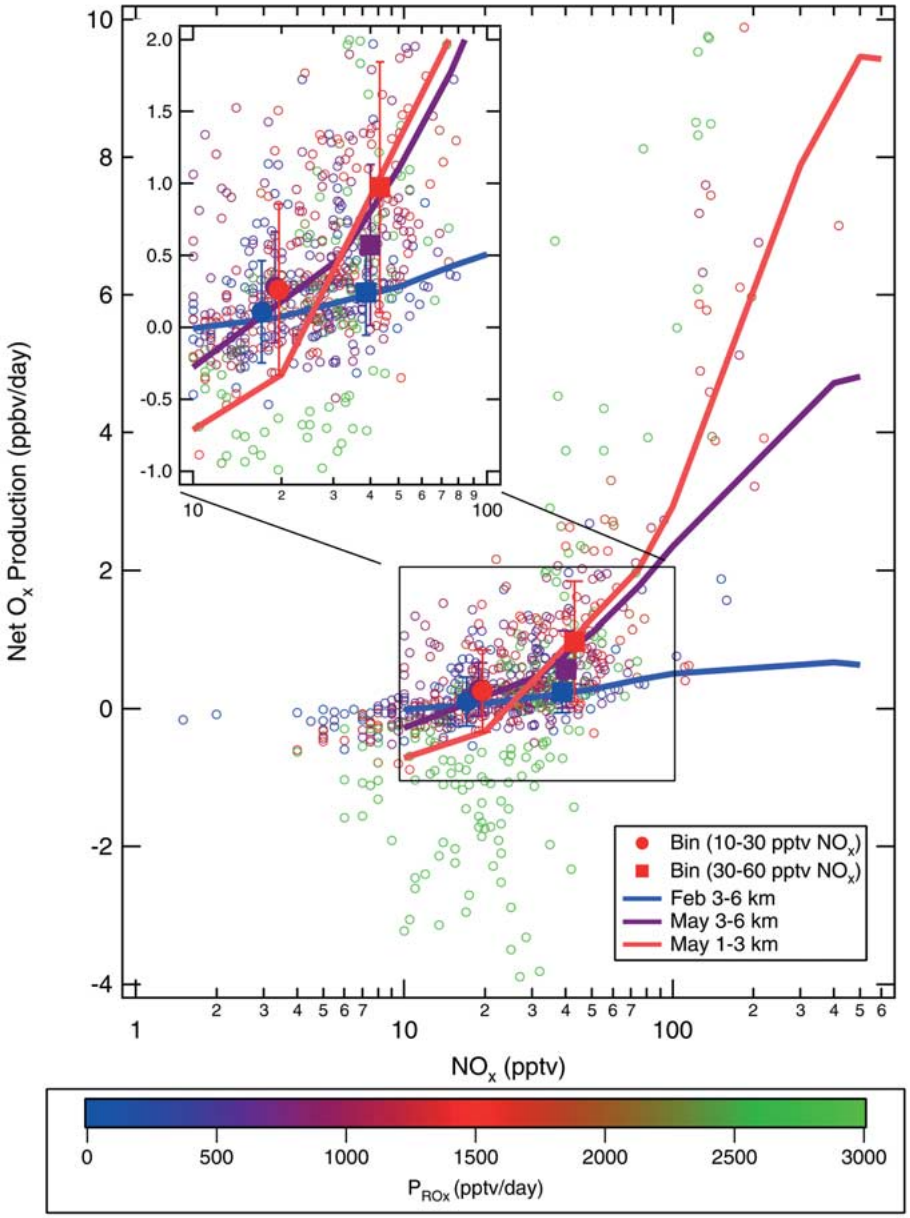

Figure 8. Dependence of net O_3 production rate (ppbv/day) on NO_x, color-coded against P_{RO_x}. Points are calculated from measurements of NO, NO_x, RO_x, H_2O, O_3, CH_2O, H_2O_2, CH_3OOH, J_{O1D} and steady-state calculations of OH and the partitioning of RO_x between HO_2 and CH_3O_2 [Cantrell *et al.*, 2003]. Data is binned based on NO_x between 10–30, 30–60 pptv for P_{RO_x} in the ranges 0–200, 600–1000, 1300–1800 pptv/day. Curves are model-derived results for various cases, color-coded against model calculated P_{RO_x}. Simulations constrained at median measured O_3, CO, H_2O, HCs, acetaldehyde, methanol, acetone, PAN, PPN, HNO_3, CH_2O, CH_3OOH, H_2O_2 with varying NO_x.

apportion HO_2 and CH_3O_2. Curves represent the results of our photochemical box model run repeatedly over the range of NO_x mixing ratios. Agreement between our modeled curves and observations is generally good for similar ranges of P_{RO_x}. For the low-light level conditions in February ($P_{RO_x} \sim 80$ pptv/day), the cross-over threshold to positive net O_3 production occurs at $NO_x \sim 10$ pptv (58–85° N, 3–6 km); by May ($P_{RO_x} \sim 1500$ pptv/day), the threshold increases to $NO_x \sim 30$ pptv (58–85° N, 1–3 km). This observation suggests that in the arctic free troposphere in the winter, the NO_x level needed to sustain net O_3 production is considerably lower than in spring. There also appears to be a dependence on altitude as the NO_x level needed to produce net O_3 is shifted to higher NO_x mixing ratios at lower altitudes. This may be an explanation for the altitude dependence seen in Figure 6, as NO_x levels are not significantly different between the 1–3 km and 3–6 km layer, especially later in the campaign.

It is also interesting to compare the sensitivity of P_{O_x} to NO_x ($d\ln(P_{O_x})/d\ln(NO_x)$) with the sensitivity of P_{O_x} to P_{RO_x} ($d\ln(P_{O_x})/d\ln(P_{RO_x})$) for the arctic free troposphere. Model runs for observations between 58–85° N yield a range of values for $d\ln(P_{O_x})/d\ln(P_{RO_x})$ between 0.50 in February and 0.38 in May, implying a fairly strong P_{O_x} dependence of P_{RO_x}. However, this sensitivity is lower than the values stated above for $d\ln(P_{O_x})/d\ln(NO_x)$ and suggests that in the arctic free troposphere while P_{O_x} increases with both NO_x and P_{RO_x}, P_{O_x} is more sensitive to the same relative change in NO_x. This comparison illustrates the importance of understanding the NO_x budget in the arctic free troposphere, as the lifetime of NO_x and thus its persistence in the arctic strongly affects the atmosphere's ability to produce O_3. The reader is referred to a companion paper for details on the NO_x budget during TOPSE (Stroud *et al.*, 2003).

4. Conclusions

The goal of this paper was to characterize the seasonal dependence of the O_x budget in the arctic free troposphere so that the following two questions could be addressed: (1) what is the importance of local photochemistry compared to transport in creating the springtime maximum in high latitude O_3 trends, and (2) what is the response of local gross and net O_3 production rates to changes in P_{RO_x} and NO_x? A photochemical box model was constrained by measured median mixing ratios based on the TOPSE observations and run to diel steady-state to calculate gross O_3 production and loss rates. The box model was run for sorted data cases based on latitude, altitude and month. This methodology was validated by comparing modeled dependencies with individual measurement points. Curves generated with the box model generally reproduced the dependence seen in the individual data points, especially for species/quantities with short equilibration times (e.g., radicals vs. $j(O^1D)$ and O_3 production rates vs. NO_x).

The radical cycling in the arctic free troposphere is considerably different from other locations, especially in winter under low actinic flux and low water vapor

mixing ratios. The majority of radical species enter and leave the radical pool as peroxy radicals. Furthermore, when peroxy radicals are converted to OH, they are very efficiently converted back to peroxy radicals. The loss mechanism of OH radicals to form HNO_3 is not efficient at the low NO_x mixing ratios typical of the arctic free troposphere. The radical production from the photolysis of aldehyde and peroxide species also dominates over O_3 photolysis. The efficiency of the radical cycling actually decreases with increasing NO_x in February. This stems from the low water vapor and low actinic flux conditions which result in low radical concentrations. Under these conditions, RO_x + NO_x reactions play and important role in removing radicals with increasing NO_x. Overall, very small radical chain lengths ($\sim$1–3) were calculated suggesting that the concept of a radical chain is not appropriate for the low NO_x conditions in the arctic mid-troposphere.

Prior modeling studies suggested a build up in the wintertime of hydrocarbons and NO_x in the arctic free troposphere followed by a 'spring cleaning' where species mixing ratios decrease due to increased rates of OH oxidation. Interestingly, while hydrocarbons decreased throughout the winter-to-spring transition, NO_x actually increased in mixing ratio between February and May, likely due to an increase in ventilation from the boundary layer. This increase in NO_x in combination with increases in radical production rates (O_3, CH_2O and peroxide photolysis) led to the springtime bloom in photochemical production of O_3. In the lower free troposphere (1–3 km), O_3 transport into the arctic free troposphere dominated the observed O_3 trend between February and March while local O_3 photochemical production dominated transport between March and May. In the middle free troposphere (3–6 km), local O_3 photochemical production dominated transport between February and May. However, the transport term was always calculated to be positive meaning that net transport of O_3 into the arctic free troposphere was needed in combination with photochemistry to reproduce the observed monthly O_3 trend. Quantitatively, our calculated gross O_3 production and loss rates are similar to results from Cantrell *et al*. (2003) and Wang *et al*. (2003) suggesting that the differences in modeling approaches (explicit vs. lumped organic chemistry, instantaneous steady-state vs. diel steady-state, point vs. median constraint) were not critical for calculating O_3 production rates in the arctic free troposphere. However, our interpretation of the results is critically different from Wang *et al.* who conclude that a small net O_3 loss (P_{O_x}–$L_{O_x}[O_x] < 0$) implies that transport must dominate over *in situ* photochemistry in explaining the springtime increase in arctic free tropospheric O_3. Fundamentally, the (P_{O_x}–$L_{O_x}[O_x]$) term can remain negative while both P_{O_x} and $L_{O_x}[O_x]$ increase significantly with season so that the P_{O_x} term surpasses the transport, T, term. Essentially, Wang *et al.* compare the T term to the (P_{O_x}–$L_{O_x}[O_x]$) term and we compare the T term to the P_{O_x} term to derive our differing conclusions.

Gross O_3 production rates were calculated to increase linearly with NO_x throughout the range of NO_x observed during TOPSE. In February, the optimum NO_x mixing ratio to maximize P_{O_x} occurs at $NO_x \sim 300$ pptv. This optimum NO_x

increased to $NO_x \sim 500$ pptv in May due to the higher P_{RO_x} rates in spring. These optimum NO_x levels are considerably lower than calculations for urban centers where $[NO_x] > 1$ ppbv are necessary to maximize P_{O_x}; however, the range of NO_x between 300–500 pptv is still more than a factor of 10 higher than the median measured values during TOPSE. The threshold for net positive O_3 production increased from $NO_x \sim 10$ pptv in February to $NO_x \sim 25$ pptv in May suggesting that the NO_x levels needed to sustain net positive O_3 production are considerably lower in winter than spring. These higher minimum NO_x levels in winter partly explain why wintertime photochemical O_3 production impacts the build-up of O_3 over winter and early spring. There is also a dependence on altitude as the NO_x threshold needed to produce net O_3 shifts to higher NO_x at lower altitudes. This likely explains why we calculate net O_3 destruction for the 1–3 km layer and net O_3 production for the 3–6 km layer. Overall, median NO_x levels observed in the arctic free troposphere are considerably lower than the NO_x levels associated with peak gross O_3 production rates. As a result, possible future increases in NO_x in the arctic free troposphere will translate into greater O_3 production throughout the winter-to-spring transition.

Acknowledgements

Special thanks to Louisa Emmons and Luca Cinquini for developing and maintaining the TOPSE data archive. C.S. would also like to thank the Advanced Study Program within the National Center for Atmospheric Research for a fellowship. NCAR is sponsored by National Science Foundation and operated by the University Corporation for Atmospheric Research. D.B., B.H. and R.T. appreciate support from the Atmospheric Sciences Division and the Office of Polar Programs of the National Science Foundation. The authors are also grateful to NCAR's Research Aviation Facility for their commitment to the TOPSE mission.

References

Atkinson, R., 1994: Gas-phase tropospheric chemistry of organic compounds, *J. Phys. Chem. Ref. Data* **R1**.

Atkinson, R., 1997a: Atmospheric reactions of alkoxy and ß-hydroxyalkoxy radicals, *Int. J. Chem. Kinet.* **29**, 99–111.

Atkinson, R., 1997b: Gas-phase tropospheric chemistry of volatile organic compounds. 1. Alkanes and alkenes, *J. Phys. Chem. Ref. Data* **26** (2), 215–290.

Atkinson, R., Baulch, D. L., Cox, R. A., Hampson, R. F., Kerr, J. A., Rossi, M. J., and Troe, J., 2000: Evaluated kinetic and photochemical data for atmospheric chemistry: Supplement VIII, halogen species – IUPAC Subcommittee on Gas Kinetic Data Evaluation for Atmospheric Chemistry, *J. Phys. Chem. Ref. Data* **29** (2), 167–266.

Atlas, E. *et al.*, 2002: TOPSE: Introduction, *J. Geophys. Res.-Atmos.*, in press.

Brune, W. H., Stevens, P. S., and Mather, J. H., 1995: Measuring OH and HO_2 in the troposphere by laser-induced fluorescence at low-pressure, *J. Atmos. Sci.* **52** (19), 3328–3336.

Cantrell, C. A., Tanner, D., Mauldin, L., and Eisele, F., 2000: Atmospheric peroxy radical measurements using chemical ionization, *Abstracts of Papers of the American Chemical Society* **219**, U309–U309.

Cantrell, C. A. *et al*., 2003: Steady-state free radical budgets and ozone photochemistry during TOPSE, *J. Geophys. Res.-Atmos.* **108** (D4), 1029/2002JD002198.

Chameides, W. and Walker, J. C. G., 1973: Photochemical theory of tropospheric ozone, *Transactions-American Geophysical Union* **54** (12), 1293–1293.

Chameides, W. L., Davis, D. D., Rodgers, M. O., Bradshaw, J., Sandholm, S., Sachse, G., Hill, G., Gregory, G., and Rasmussen, R., 1987: Net ozone photochemical production over the eastern and central north Pacific as inferred from GTE CITE-1 observations during fall 1983, *J. Geophys. Res.-Atmos.* **92** (D2), 2131–2152.

Christensen, L. E., Okumura, M., Sander, S.P, Salawitch, R. J., Toon, G. C., Sen, B., Blavier, J.-F., and Jucks, K. W., 2002: Kinetics of HO_2+HO_2?H_2O_2+O_2: Implications for stratospheric H_2O_2, *Geophys. Res. Lett.* **29**.

Crawford, J. *et al*., 1999: Assessment of upper tropospheric HO_x sources over the tropical Pacific based on NASA GTE/PEM data: Net effect on HO_x and other photochemical parameters, *J. Geophys. Res.-Atmos.* **104**, 16255–16273.

Crutzen, P. J., 1974: Photochemical reactions initiated by and influencing ozone in unpolluted tropospheric air, *Tellus* **26** (1–2), 47–57.

Demore, W. B. *et al.*, 1997: Chemical kinetics and photochemical data for use in stratospheric modeling, *JPL Publications* 97–4.

Eisele, F. L., Tanner, D. J., Cantrell, C. A., and Calvert, J. C., 1997: Measurements and steady-state calculations of OH concentrations at Mauna Loa Observatory, *J. Geophys. Res.-Atmos.* **101**, 14665–14679.

Elterman, L., UV, visible and IR attenuation for altitudes to 50 km,
AFCRL-68–0153, No. 285, Air Force Cambridge Research Laboratories, Bedford, MA, 1968.

Emmons, L. K. *et al*., 2002: The budget of tropospheric ozone during TOPSE from two CTMs, *J. Geophys. Res.-Atmos.*, in press.

Follows, M. J. and Austin, J. F., 1992: A zonal average model of the stratospheric contributions to the tropospheric ozone budget, *J. Geophys. Res.-Atmos.* **97** (D16), 18047–18060.

Fried, A. *et al*., 2002: Tunable diode laser measurements of formaldehyde during TOPSE 2000 study: Distributions, trends and model comparisons, *J. Geophys. Res. Atmos.*, in press.

Frost, G. J., Trainer, M., Mauldin III, R. L., Eisele, F. L., Prevot, A. S. H., Flocke, S. J., Madronich, S., Kok, G., Schillawski, R. D., Baumgardner, D., and Bradshaw, J., 1999: Photochemical modeling of OH levels during the First Aerosol Characterization Experiment (ACE 1), *J. Geophys. Res.-Atmos.* **104** (D13), 16041–16052.

Jacob, D. J., Heikes, B. G., Fan, S. M., Logan, J. A., Mauzerall, D. L., Bradshaw, J. D., Singh, H. B., Gregory, G. L., Talbot, R. W., Blake, D. R., and Sachse, G. W., 1996: Origin of ozone and NO_x in the tropical troposphere: A photochemical analysis of aircraft observations over the South Atlantic basin, *J. Geophys. Res.-Atmos.* **101** (D19), 24235–24250.

Jaegle, L., Jacob, D. J., Brune, W. H., Faloona, I., Tan, D., Heikes, B. G., Kondo, Y., Sachse, G. W., Anderson, B., Gregory, G. L., Singh, H. B., Pueschel, R., Ferry, G., Blake, D. R., and Shetter, R. E., 2000: Photochemistry of HO_x in the upper troposphere at northern midlatitudes, *J. Geophys. Res.-Atmos.* **105** (D3), 3877–3892.

Junge, C. E., 1962: Global ozone budget and exchange between stratosphere and troposphere, *Tellus* **14**, 363–377.

Kanaya, Y., Matsumoto, J., Kato, S., and Akimoto, H., 2001: Behavior of OH and HO_2 radicals during the Observations at a Remote Island of Okinawa (ORION99) field campaign 2. Comparison between observations and calculations, *J. Geophys. Res.-Atmos.* **106** (D20), 24209–24223.

Klonecki, A. and Levy, H., 1997: Tropospheric chemical ozone tendencies in CO-CH_4-NO_y-H_2O system: Their sensitivity to variations in environmental parameters and their application to a global chemistry transport model study, *J. Geophys. Res.-Atmos. 102* (D17), 21221–21237.

Kotchenruther, R. A., Jaffe, D. A., and Jaegle, L., 2001: Ozone photochemistry and the role of peroxyacetyl nitrate in the springtime northeastern Pacific troposphere: Results from the Photochemical Ozone Budget of the Eastern North Pacific Atmosphere (PHOBEA) campaign, *J. Geophys. Res.-Atmos.* **106** (D22), 28731–28742.

Levy, H., 1971: Normal atmosphere: Large radical and formaldehyde concentrations predicted, *Science* **173**, 141–143.

Levy, H., Mahlman, J. D., Moxim, W. J., and Liu, S. C., 1985: Tropospheric ozone – the role of transport, *J. Geophys. Res.-Atmos.* **90** (ND2), 3753–3772.

Levy, H. I., Kasibhatla, P. S., Moxim, W. J., Klonecki, A. A., Hirsch, A. I., Oltmans, S. J., and Chameides, W. L., 1997: The human impact on global tropospheric ozone, *Geophys. Res. Lett.* **24**, 791–794.

Logan, J. A., 1985: Tropospheric ozone – seasonal behavior, trends, and anthropogenic influence, *J. Geophys. Res.-Atmos.* **90** (ND6), 463–482.

Madronich, S. and Calvert, J. G., 1990: Permutation reactions of organic peroxy radicals in the troposphere, *J. Geophys. Res.-Atmos.* **95** (D5), 5697–5715.

Madronich, S. and Flocke, S., 1998: The role of solar radiation in atmospheric chemistry, in P. Boule (ed.), *Handbook of Environmental Chemistry*, Springer-Verlag, Heidelberg, Springer-Verlag, Heidelberg, pp. 1–26.

Mauzerall, D. L., Jacob, D. J., Fan, S. M., Bradshaw, J. D., Gregory, G. L., Sachse, G. W., and Blake, D. R., 1996: Origin of tropospheric ozone at remote high northern latitudes in summer, *J. Geophys. Res.-Atmos.* **101** (D2), 4175–4188.

Mereau, R., Rayez, M. T., Caralp, F., and Rayez, J. C., 2000: Theoretical study of alkoxyl radical decomposition reactions: Structure-activity relationships, *Physical Chemistry Chemical Physics* **2** (17), 3765–3772.

Monks, P. S., 2000: A review of the observations and origins of the spring ozone maximum, *Atmos. Environ.* **34** (21), 3545–3561.

Muller, J. F. and Brasseur, G., 1995: IMAGES – A 3-dimensional chemical-transport model of the global troposphere, *J. Geophys. Res.-Atmos.* **100** (D8), 16445–16490.

Oltmans, S. J., Hofmann, D. J., Lathrop, J. A., Harris, J. M., Komhyr, W. D., and Kuniyuki, D., 1996: Tropospheric ozone during Mauna Loa observatory photochemistry experiment 2 compared to long-term measurements from surface and ozonesonde observations, *J. Geophys. Res.-Atmos.* **101** (D9), 14569–14580.

Orlando, J. J., Tyndall, G. S., Bilde, M., Ferronato, C., Wallington, T. J., Vereecken, L., and Peeters, J., 1998: Laboratory and theoretical study of the oxy radicals in the OH- and Cl-initiated oxidation of ethene, *J. Phys. Chem. A* **102**, 8116–8123.

Ridley, B. A., Madronich, S., Chatfield, R. B., Walega, J. G., Shetter, R. E., Carroll, M. A., and Montzka, D. D., 1992: Measurements and model simulations of the photostationary state during the Mauna-Loa-Observatory Photochemistry Experiment – Implications for radical concentrations and ozone production and loss rates, *J. Geophys. Res.-Atmos.* **97** (D10), 10375–10388.

Reeves, C. E. *et al*., 2002: Potential for photochemical ozone formation in the troposphere over the North Atlantic as derived from aircraft observations during ACSOE, *J. Geophys. Res.-Atmos.* **107** (D23), art. no. 4707.

Roelofs, G. and Lelieveld, J., 1995: Distribution and budget of O_3 in the troposphere calculated with a chemistry general circulation model, *J. Geophys. Res.-Atmos.* **100**, 20983–20998.

Sander, S. P. *et al*., 2000: Chemical kinetics and photochemical data for use in stratospheric modeling, *JPL Publications* 00–3.

Seinfeld J. H. and Pandis, S. N., 1998: Atmospheric chemistry and physics: From air pollution to climate change, *Wiley-Interscience*.

Schultz, M., *et al*., 1999: On the origin of tropospheric ozone and NO_x over the tropical South Pacific, *J. Geophys. Res.-Atmos.* **104**, 5829–5843.

Singh, H., 2001: Evidence from the Pacific troposphere for large global sources of oxygenated organic compounds, *Nature* **410** (6832), 1078–1081.

Stroud, C. A. *et al*., 2003: Photochemistry in the arctic free troposphere: NO_x budget and the role of odd nitrogen reservoir recycling, *Atmos. Environ.* **37**, 3351–3364.

Tanimoto, H. *et al*., 2002: Seasonal cycles of ozone and oxidized nitrogen species in northeast Asia – 2. A model analysis of the roles of chemistry and transport, *J. Geophys. Res.-Atmos.* **107** (D23), art. no. 4706.

Thornton, J. A. *et al*., 2002: Ozone production rates as a function of NO_x abundances and HO_x production rates in the Nashville urban plume, *J. Geophys. Res.-Atmos.* **107** (D12).

Tyndall, G. S., Cox, R. A., Granier, C., Lesclaux, R., Moortgat, G. K., Pilling, M. J., Ravishankara, A. R., and Wallington, T. J., 2001: Atmospheric chemistry of small organic peroxy radicals, *J. Geophys. Res.-Atmos.* **106** (D11), 12157–12182.

Wang Y. *et al*., 2003: Springtime photochemistry at northern mid and high latitudes, *J. Geophys. Res.-Atmos.* **108** (D4), 1029/2002JD002227.

Yienger, J. J., Klonecki, A. A., Levy II, H., Moxim, W. J., and Carmichael, G. R., 1999: An evaluation of chemistry's role in the winter-spring ozone maximum found in the northern midlatitude free troposphere, *J. Geophys. Res.-Atmos.* **104** (D7), 8329–8329.

Zanis, P., Monks, P. S., Schuepbach, E., and Penkett, S. A., 1999: On the relationship of HO2+RO2 with j((OD)-D-1) during the Free Tropospheric Experiment (FREETEX '96) at the Jungfraujoch Observatory (3580 m above sea level) in the Swiss Alps, *J. Geophys. Res.-Atmos.* **104** (D21), 26913–26925.

Zanis, P., Monks, P. S., Schuepbach, E., and Penkett, S. A., 2000: The role of in situ photochemistry in the control of O_3 during spring at the Jungfraujoch (3580 m asl) – Comparison of model results with measurements, *J. Atmos. Chem.* **37** (1), 1–27.

Zanis, P. *et al*., 2003: Seasonal variation of peroxy radicals in the lower free troposphere based on observations from the FREE Tropospheric Experiments in the Swiss Alps, *Geophys. Res. Lett.* **30** (10), art. no. 1497.